The Dynamics of a Barotropic Current Impinging on an Ice Front

NADINE STEIGER,[a,b] ELIN DARELIUS,[a,b] SATOSHI KIMURA,[c] RYAN D. PATMORE,[d,e] AND ANNA K. WÅHLIN[f]

[a] Geophysical Institute, University of Bergen, Bergen, Norway
[b] Bjerknes Center for Climate Research, Bergen, Norway
[c] Japan Agency for Marine-Earth Science and Technology, Yokosuka, Japan
[d] British Antarctic Survey, Cambridge, United Kingdom
[e] University of Reading, Reading, United Kingdom
[f] Department of Marine Sciences, University of Gothenburg, Gothenburg, Sweden

ABSTRACT: The vertical front of ice shelves represents a topographic barrier for barotropic currents that transport a considerable amount of heat toward the ice shelves. The blocking effect of the ice front on barotropic currents has recently been observed to substantially reduce the heat transport into the cavity beneath the Getz Ice Shelf in West Antarctica. We use an idealized numerical model to study the vorticity dynamics of an externally forced barotropic current at an ice front and the impact of ice shelf thickness, ice front steepness, and ocean stratification on the volume flux entering the cavity. Our simulations show that thicker ice shelves block a larger volume of the barotropic flow, in agreement with geostrophic theory. However, geostrophy breaks locally at the ice front, where relative vorticity and friction become essential for the flow to cross the discontinuity in water column thickness. The flow entering the cavity accelerates and induces high basal melt rates in the frontal region. Tilting the ice front, as undertaken in sigma-coordinate models, reduces this acceleration because the flow is more geostrophic. Viscous processes—typically exaggerated in low-resolution models—break the potential vorticity constraint and bring the flow deeper into the ice shelf cavity. The externally forced barotropic current can only enter the cavity if the stratification is weak, as strong vertical velocities are needed at the ice front to squeeze the water column beneath the ice shelf. If the stratification is strong, vertical velocities are suppressed and the barotropic flow is almost entirely blocked by the ice front.

SIGNIFICANCE STATEMENT: Ice shelves in West Antarctica are thinning, mostly from basal melting through oceanic heat entering the underlying ice shelf cavities. Thinning of ice shelves reduces their ability to buttress the grounded ice resting upstream, leading to sea level rise. To model the ice sheet's contribution to sea level rise more accurately, the processes governing the oceanic heat flux into the ice shelf cavity must be articulated. This modeling study investigates the dynamics of a depth-independent current approaching the ice shelf; it corroborates previous findings on the blocking of such a current at the ice front. The amount of water that enters the cavity strongly depends on ice shelf thickness and ocean stratification. For a well-mixed ocean, the upper part of the flow can dive underneath the ice shelf and increase basal melting near the ice front. In a stratified ocean, the approaching depth-independent current is almost entirely blocked by the ice front.

KEYWORDS: Ice shelves; Barotropic flows; Ocean dynamics; Potential vorticity; Topographic effects; Idealized models

1. Introduction

Basal melting is a central component of the mass budget of ice shelves in West Antarctica. It is induced by relatively warm ocean water that flows into the sub-ice shelf cavities and melts the base of the floating ice (Pritchard et al. 2012; Rignot et al. 2013). In West Antarctica, the ocean heat mainly originates from warm and saline Circumpolar Deep Water (CDW; Orsi et al. 1995) north of the continental shelf. The warm water is transported onto the continental shelf and toward the ice shelves (Wåhlin et al. 2010; Jacobs et al. 2012; Arneborg et al. 2012) by oceanic currents that have both a barotropic (depth constant; set up by gradients in the sea surface height) and a baroclinic (depth varying; set up by horizontal density gradients) component (Arneborg et al. 2012; Kalén et al. 2016; Wåhlin et al. 2020). Recent observations in front of the western Getz Ice Shelf (see Fig. 1) revealed that about 70% of the heat flux toward the ice shelf is associated with the barotropic component of the flow (Wåhlin et al. 2020). This barotropic component is topographically blocked and deflected at the vertical ice front that protrudes several hundred meters into the ocean (Wåhlin et al. 2020). The theory of topographic blocking assumes geostrophically balanced, barotropic flow (Wåhlin et al. 2020) and hence that potential vorticity (PV) is dominated by f/H. In that case, the
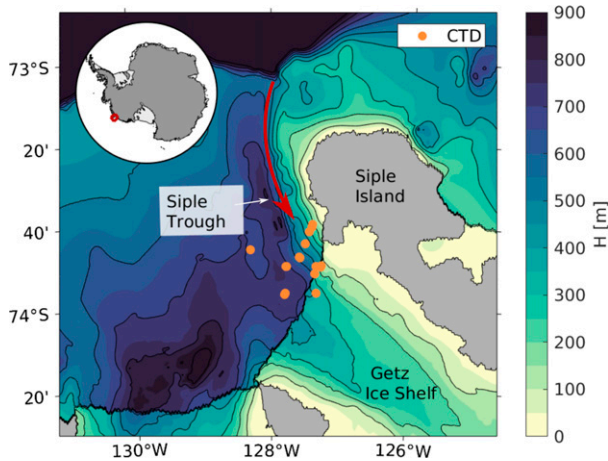
FIG. 1. Map of the water column thickness H from RTOPO2 (Schaffer et al. 2016) on the continental shelf around Siple Trough and below the Getz Ice Shelf. Black contours are at 100-m intervals, and grounded ice/land is shaded in gray. Shown are also the locations of CTD stations (orange circles; Assmann et al. 2019) and the inflow suggested by Assmann et al. (2019) (red arrow). The inset shows the Antarctic continent, with the location of the map marked by a red square.

flow follows lines of constant water column thickness H, given small variations in latitude represented by the Coriolis parameter f (Cushman-Roisin and Beckers 2011). At the ice front, the water column thickness changes abruptly and f/H contours converge. Here, relative vorticity and friction play an increased role in the vorticity budget, and the flow can consequently deviate from f/H contours. A detailed understanding of the topographic influence of an ice front on the dynamics of a barotropic current is still lacking.

Barotropic currents in the presence of a topographic step have been studied in various idealized settings. For example, laboratory experiments and idealized numerical modeling showed that turbulent barotropic flow over a flat bottom with a topographic step organizes itself into two large opposed vortices that are separated by the step (Tenreiro et al. 2010). Further idealized studies of a barotropic coastal current that encounters a topographic step perpendicular to the coast find different dynamic responses of the current to the topographic step depending on the size of the step and whether the topography is shoaling or deepening across the step (Carnevale et al. 1999; Sansón et al. 2005). Depending on the configuration, the current might be entirely diverted at the step topography or it may bifurcate, with the deflected part either following the topographic step or forming a dipolar jet that returns back upstream due to the tendency of the deflected flow to align with shallow water to the left or right in the Southern or Northern Hemisphere, respectively. In the context of an ice shelf cavity, where the ice front imposes a step in the water depth from above and not from below, Stern et al. (2014) found that a circulation cell develops inside the cavity, largely isolated from outside the cavity. They observed cross exchange between the ice shelf cavity and the surrounding ocean only through baroclinic

flow induced by a dense current that enters the cavity at the bottom and a fresh meltwater plume that exits the cavity at the surface. Grosfeld et al. (1997) reproduced the topographic barrier between the ice shelf cavity and the adjacent ocean with a coarse-resolution (0.1°–0.3°) model and showed that a barotropic flow can cross the barrier where a sloping bottom topography crosses the ice front. While topographic blocking at the ice front has been observed in front of the Getz Ice Shelf (Wåhlin et al. 2020), and at the Ronne Ice Shelf in the Weddell Sea (Foldvik et al. 2001), the study by Grosfeld et al. (1997) remains the only modeling study that investigates the impact of the ice front on an externally forced barotropic flow.

Many relevant idealized modeling studies (e.g., Determann and Gerdes 1994; Losch 2008; Holland 2017) have rather focused on a baroclinic cavity circulation related to the so-called ice pump (Lewis and Perkin 1986), which is driven by ice shelf melting at depth due to the reduced freezing point and the rise of meltwater along the ice shelf base. A regional modeling study by Jourdain et al. (2017) showed that enhanced basal melting strengthens an alongshore barotropic coastal current and that the melt-induced volume transport into a cavity is 100–500 times as strong as the melt volume flux itself. However, there has been no high-resolution modeling study that explicitly investigates how much of an externally forced barotropic flow can enter the ice shelf cavity under different ice shelf and ocean conditions.

Barotropic currents in the Antarctic shelf seas are typically driven by winds (Kusahara and Ohshima 2009) or by tides (Padman et al. 2018). Tidally induced barotropic currents are strong in the Weddell Sea (Padman et al. 2018) but weak in the Amundsen Sea (Robertson 2013). Wind-driven barotropic currents along the coast occur both on short time scales of less than a few days through the generation of coastal trapped waves (Wåhlin et al. 2016) and on intraseasonal time scales (3–100 days) (McKee and Martinson 2020). The barotropic currents flow along the slope of the continental shelf and the coast, following f/H contours. A southward deflection of the along-slope currents onto the continental shelf occurs where troughs cross cut the continental shelf, reducing the topographic barrier (Williams et al. 2001; Walker et al. 2007; St-Laurent et al. 2013). The diversion of the barotropic flow into the troughs depends on the relative vorticity and the strength of the topography, determined by the curvature at the entrance of the trough (Dinniman and Klinck 2004; Williams et al. 2001). Southward barotropic flow toward the ice shelves along the eastern flank of such troughs has been observed, for example, in the Siple Trough leading to the Getz Ice Shelf (Wåhlin et al. 2020) and in the Dotson–Getz Trough (Kalén et al. 2016). It is unclear how the steepness and thickness of the ice front influence the barotropic flow into ice shelf cavities.

In this study, we investigate the vorticity dynamics of a barotropic flow near the ice front and quantify the degree of topographic blocking under different ice shelf configurations and ocean stratification. The results are based on idealized model simulations of an externally forced barotropic current approaching an ice shelf along the slope of a trough in a cyclonic direction. Such a circulation is typical on the Amundsen Sea continental shelf (Ha et al. 2014; Kalén et al. 2016). The

idealized setup is inspired by the laboratory experiments presented in Wåhlin et al. (2020) and expanded to a scale relevant for ice shelf systems like the Getz Ice Shelf over the Siple Trough (Fig. 1). The synthetic trough and ice shelf configuration allow us to conduct a range of sensitivity experiments. We start with a homogeneous ocean and systematically vary model resolution and ice shelf geometry. The ice shelf geometry dictates the strength of the topographic barrier, which we modify through changes in the ice shelf draft and the steepness of the ice front. Then, we include a linear stratification in salinity (while keeping an externally forced barotropic current) and investigate its impact on the volume flux into the ice shelf cavity. Ice shelf melting is turned off in the model simulations in order to focus on the dynamics of the barotropic flow, but the results are complemented with simulations including ice shelf melting.

2. Methods

a. Model specifications

We conduct idealized ocean–ice shelf simulations using the MITgcm ocean model (Adcroft et al. 2018) with the implemented ice shelf package (Losch 2008). The MITgcm is a z-level model that allows the treatment of the ice front as a vertical wall. In our configuration, the ocean model is hydrostatic and Boussinesq. The solved equations in a rotating Cartesian coordinate system (x, y, z) are given by

$$\frac{D\mathbf{u}}{Dt} + f\mathbf{k} \times \mathbf{u} = -\frac{1}{\rho_0}\nabla_h p + A_h \nabla_h^2 \mathbf{u} + A_r \frac{\partial^2 \mathbf{u}}{\partial z^2} + \frac{\partial \boldsymbol{\tau}_d}{\partial z}, \quad (1)$$

$$\rho g = -\frac{\partial p}{\partial z}, \quad (2)$$

$$\nabla_h \cdot \mathbf{u} = -\frac{\partial w}{\partial z}, \quad (3)$$

$$\frac{D\Theta}{Dt} = Q_\Theta, \quad \text{and} \quad (4)$$

$$\frac{DS}{Dt} = Q_S, \quad (5)$$

where $\mathbf{u} = (u, v)$ is the horizontal velocity and w is the vertical velocity, D/Dt is the total derivative, and $\mathbf{k}$ is the vertical unit vector. The variable p is the pressure, and g is the gravitational acceleration. The density $\rho = \rho_0[1 - \alpha(\Theta - \Theta_0) + \beta(S - S_0)]$ is a linear function of potential temperature Θ and salinity S, which are advected following the tracer equations (4) and (5), where the source and sink terms Q_Θ and Q_S include diffusion terms. We apply the Laplacian diffusion in the vertical and horizontal. The constants ρ_0, Θ_0, and S_0 are the reference density, temperature, and salinity, respectively, and the variables α and β are the coefficients for thermal expansion and haline contraction. The parameters A_h and A_r are the horizontal and vertical eddy viscosity parameters, respectively. The horizontal eddy viscosity aims to reproduce subgrid processes not resolved with the model. Its value is chosen in agreement with the Prandtl's mixing theory (Prandtl 1925)

and as small as numerical stability allows. The values for A_h and A_r used here have been tested in similar setups (e.g., Holland 2017). No-slip conditions at the bottom and the base of the ice shelf are represented by a quadratic drag $\boldsymbol{\tau}_d = C_d|\mathbf{u}|\mathbf{u}$ in the cells adjacent to the ice and the bottom topography with a drag coefficient $C_d = 0.0025$, following, for example, MacAyeal (1984) and Årthun et al. (2013). We tested formulations with a linear drag to see if it had any bearing on the dynamics (not shown), which gave a negligible difference in velocities and vorticity dynamics when compared with the simulations with a quadratic drag. Free-slip conditions are used at the sides and at the vertical face of the ice front following, for example, Holland (2017), because frictional processes at the lateral boundaries are not well resolved with our horizontal resolution. The sloping topography of the bed and the ice shelf base are represented with partial cells (Adcroft et al. 1997).

In the simulations with ice shelf melting enabled, melt rates are calculated using the three-equation model, which links the local freezing relation and the balance of heat and salt fluxes at the ice–ocean interface (Jenkins et al. 2001). We use a velocity-dependent transfer coefficient for salt and temperature (Holland and Jenkins 1999). The values used for constant model parameters are given in Table 1.

The model equations are solved on a third-order direct space–time, flux-limiter advection scheme. The free surface boundary condition is calculated from the linearized version of the depth-integrated continuity equation. The model simulations are spun up from rest, and we present averages of the last two days of the model output, when the system is in a quasi steady state in which the kinetic energy is changing less than 1%. The homogeneous experiments and those with melting turned on are run for about 100 days, and the stratified experiments are run for 240 days.

b. Experimental setup: The control run

The idealized geometry of the trough and the ice shelf is inspired by the laboratory experiments presented by Wåhlin et al. (2020). This setting—a trough cross-cutting the continental shelf leading up to an ice shelf—is typical around Antarctica (see, e.g., the Siple Trough leading to the Getz Ice Shelf; Fig. 1). The rectangular model domain has a size of 240 km $\times$ 120 km $\times$ 650 m and is shown in Fig. 2a. We use a horizontal resolution of $dx = dy = 500$ m in the control run (CTRL), a vertical resolution of $dz = 5$ m in the vertical direction, and a time step of $dt = 120$ s. The bathymetry consists of a symmetric channel that has a flat bottom in the center and linearly sloping sides (1.3% slope) that transition onto a horizontal continental shelf (Fig. 2a). The flat center of the channel is 650 m deep and 40 km wide, and the continental shelf is 300 m deep and 20 km wide on both sides. As a representation of the shelf break, the continental shelf slopes down from 300-m depth at $x = -155$ km toward 650-m depth at the boundary at $x = x_{\min} = -180$ km. The channel is overlaid by an ice shelf with the vertical ice front located at $x = 0$. The ice shelf draft h_{is} increases linearly with x by 0.5% from $h_0 = 300$ m at the ice front (in the CTRL). The resulting water column thickness $H = h_b + \eta - h_{is}$ is given by

TABLE 1. List of constant model parameters.

Parameter	Description	Value	Unit
f	Coriolis parameter at the lat $\phi = -73.5°$	-1.398×10^{-4}	s^{-1}
g	Gravitational acceleration	9.81	$m\ s^{-2}$
ρ_0	Reference density	1027.5	$kg\ m^{-3}$
T_0	Reference background temperature	0	°C
S_0	Reference background salinity	34.3	psu
α	Thermal expansion coef	5.02×10^{-5}	$°C^{-1}$
β	Haline expansion coef	7.86×10^{-4}	psu^{-1}
A_h	Lateral eddy viscosity	25	$m^2\ s^{-1}$
A_r	Vertical eddy viscosity	1×10^{-4}	$m^2\ s^{-1}$
C_d	Bottom and ice shelf drag coef	0.0025	
diffKrT	Vertical diffusion of temperature	1×10^{-5}	$m^2\ s^{-1}$
diffKhT	Laplacian diffusion of heat laterally	5	$m^2\ s^{-1}$
diffKrS	Vertical diffusion of salinity	1×10^{-5}	$m^2\ s^{-1}$
diffKhS	Laplacian diffusion of salt laterally	5	$m^2\ s^{-1}$
κ	Temperature diffusion coef of the ice shelf	1.54×10^{-6}	$m^2\ s^{-1}$
ρ_I	Density of the ice shelf	917	$kg\ m^{-3}$
hFacMin	Min fraction size of a cell	0.2	
hFacSup	Max fraction size of a cell	2	

the distance between the bed topography h_b and the free surface displacement η, minus the ice shelf draft. The water column thickness for the CTRL is presented in Fig. 2b.

We prescribe a barotropic inflow along the boundaries at $y = y_{max} = 60$ km and an outflow at $y = -y_{max}$. A depth-constant velocity field with a sinusoidal profile is used at the inflow and outflow over the shelf break (Fig. 2b) according to

$$v(x)\big|_{y=\pm y_{max}} = \begin{cases} -v_0 \sin\left[\dfrac{\pi(x - x_{min})}{l}\right], & \text{for } x \le x_{min} + l \\ 0, & \text{for } x > x_{min} + l \end{cases}.$$

The core velocity is $v_0 = 0.1$ m s^{-1}, and the width of the current is $l = 25$ km. In the control simulation, temperature and salinity are uniform in time and space and set to $T = 0°C$ and $S = 34.3$ psu, respectively.

c. Experimental setup: Sensitivity runs

After analyzing the dynamics of the current in the CTRL, we test the sensitivity of the results to model resolution, geometric changes of the ice shelf, and stratification. The parameters for the model experiments used in this study are listed in Table 2.

We examine the model sensitivity to horizontal resolution by changing the horizontal grid size in a range from 100 to 2000 m (run02–run05). The horizontal eddy viscosity parameter is scaled linearly with grid size according to mixing-length theory and to ensure numerical stability. Then, we study geometric effects by changing the ice shelf draft by increasing h_0 in a range from 0 to 650 m (keeping the slope of the ice shelf base constant; run06–run10) and by changing the slope of the ice front from vertical to three percent by increasing the width of the ice front W from 0 to 5 and 10 km (run11 and run12) (Fig. 2c). The sloping ice front is comparable to what is used in sigma-coordinate models, for example, the Regional Ocean Modeling System (ROMS) with a slope of $h_0/W = 4\%$ at the Filchner–Ronne Ice Shelf (e.g., Huneke et al. 2019).

In the experiments with varying stratification (run13–run17), we use a linear stratification in salinity (temperature is kept constant) and increase it systematically. Stratification is quantified by the Brunt–Väisälä frequency, $N^2 = -(g/\rho_0)(\partial\rho/\partial z)$, and we vary the stratification within a range of $N = 0 - 3.4 \times 10^{-3}$ s^{-1}. This covers a broad range of Burger numbers, Bu $= N^2\mathscr{H}^2/(f^2\mathscr{L}^2) = 0$–1.8, using a length scale of $\mathscr{L} = 10^4$ m and a vertical scale of $\mathscr{H} = 550$ m. The Burger number expresses the relative importance of stratification versus rotation (Cushman-Roisin and Beckers 2011). Hydrographic profiles from the Siple Trough show an almost linear density profile in the depth range of 100–500 m, with stratification in the range of $N = 0.2 \times 10^{-3}$–2.9×10^{-3} s^{-1} (Bu $= 0$–1.3) (Fig. 2d). The first 17 model experiments are conducted with ice shelf melt turned off. We also investigate the impact on basal melt in experiments with and without barotropic forcing and stratification (run18–run21).

d. Potential vorticity and continuity

We use the barotropic potential vorticity equation to analyze the vorticity dynamics in the homogeneous case. The equation is obtained by taking the curl of the depth-integrated momentum equation divided by H (Hughes 2008) and can be rearranged to

$$\frac{D}{Dt}\left(\frac{f + \zeta}{H}\right) = F, \tag{6}$$

where $\zeta = \mathbf{k} \cdot \nabla \times \overline{\mathbf{u}} = (\partial\overline{v}/\partial x) - (\partial\overline{u}/\partial y)$ is the relative vorticity of the depth-averaged flow; F (hereinafter the "friction term") is the sink/source term of potential vorticity in a homogeneous ocean that includes viscous processes, drag at the lower and upper boundary, and vertical shear generated by vertical nonuniformity in friction at the ice front (see the appendix). The viscous term represents the internal stress and accounts for subgrid-scale dynamics that are unresolved. The effect of viscosity will be discussed further in section 4a in connection with the model resolution. The bottom stress is parameterized by the quadratic drag law in the boundary cells of the model and is
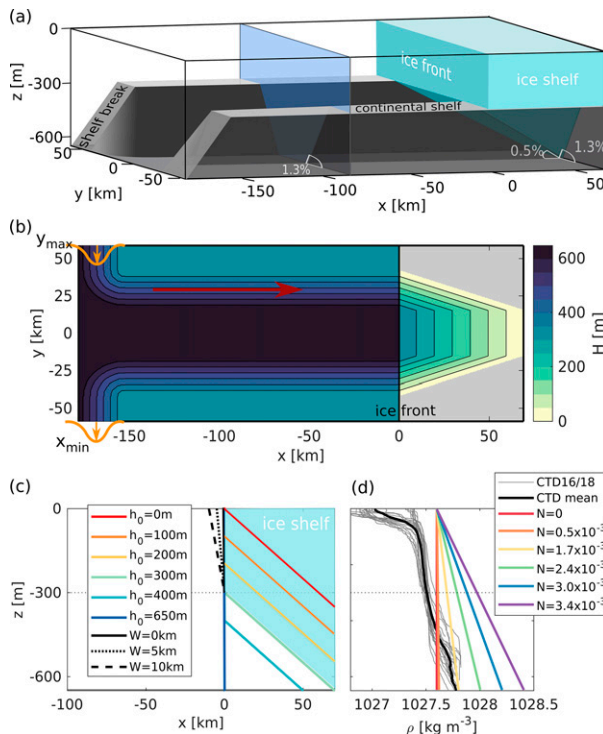
FIG. 2. (a) Model domain and geometry of the idealized bed (gray) and ice shelf (cyan) used in the CTRL. The transparent blue area highlights the channel geometry in a cross section. (b) Water column thickness H for the CTRL; contours with $H > 350$ m are blocked at the ice front. Orange arrows and curve show the forced barotropic velocities at the inflow and outflow along the shelf break, and the red arrow sketches the flow toward the ice shelf. (c) Ice shelf geometries for the model experiments with varying ice shelf draft h_0 (run06–run10) and ice front width W (run11 and run12). The ice shelf in the CTRL ($h_0 = 300$ m; $W = 0$ m) is shaded in cyan. (d) Individual (light gray) and averaged (thick black) density profiles from CTD observations from January 2016 and 2018 (see locations in Fig. 1) together with density profiles of the stratification runs for different N (s^{-1}) (run13–run17).

expected to create an Ekman transport to the right of the interior flow, both along the bed topography and at the ice shelf base (e.g., Cushman-Roisin and Beckers 2011). Ekman pumping occurs in regions where the Ekman transport diverges or converges, leading to a source or sink of potential vorticity, respectively, which is contained in the vertical shear terms. Although the frictional terms contained in F are dynamically distinct, it is their net effect that is of interest here.

In the homogeneous case, the pressure term in the momentum budget vanishes during the calculation of the potential vorticity budget. In the model simulations with stratification, isopycnals get tilted at the ice front and a baroclinic component of the flow develops. While the vorticity dynamics of the stratified runs is not analyzed here, we note that the inclusion of a baroclinic flow adds an additional term to the vorticity budget.

The depth-integrated continuity equation of an incompressible fluid in steady state (3) is given by

$$\nabla_h \cdot \mathbf{U} = 0, \tag{7}$$

with the depth-integrated volume transport

$$\mathbf{U} = \int_{-h_b}^{\eta - h_{is}} \mathbf{u}\, dz = H\overline{\mathbf{u}}.$$

The continuity equation allows the use of a barotropic streamfunction Ψ that is defined such that $\mathbf{U} = \mathbf{k} \times \nabla\Psi$. The depth integration eliminates vertical velocities that occur through horizontal convergence or divergence. In our setup, the flow in x direction converges at the ice front, and the flow in y direction converges at the sloping walls of the channel. The horizontal convergence of the barotropic flow leads to vertical velocities that vary linearly with depth. The magnitude of the vertical velocities at the bottom (w_{-h_b}) and at the upper boundary ($w_{\eta - h_{is}}$) can be estimated from kinematic boundary conditions in steady state (Cushman-Roisin and Beckers 2011), ignoring the contribution from viscous topographic effects (Sansón and Heijst 2002), which is two orders of magnitude smaller at the ice front:

$$w|_{-h_b} = \mathbf{u} \cdot \nabla(-h_b) = -v(\partial h_b/\partial y) \quad \text{and} \tag{8}$$

$$w|_{\eta - h_{is}} = \mathbf{u} \cdot \nabla(\eta - h_{is}) \approx -u\frac{\partial h_{is}}{\partial x}, \tag{9}$$

where we used that $\partial h_b/\partial x = 0$, $\partial(\eta - h_{is})/\partial y \approx 0$, and $\partial(\eta - h_{is})/\partial x \approx \partial h_{is}/\partial x$ in our setup, considering changes in η to be small. The gradient of the bathymetry is $|\partial h_b/\partial y| = 0.013$ along the sloping walls of the channel and $\partial h_b/\partial y = 0$ in the center of the channel. The gradient of the upper boundary within the ice shelf cavity is the slope of the ice shelf base $\partial h_{is}/\partial x = 0.005$, and at the ice front the gradient is given by the draft of the ice front over the width of the ice front, that is, h_0/W. For the vertical front, the width corresponds to the grid size such that $h_0/W = h_0/dx = 0.6$ in the control run.

e. Volume fluxes for the quantification of blocking

We quantify the amount of topographic blocking by comparing the volume flux approaching the ice shelf Q_g with the blocked volume flux that is deflected at the ice front Q_b and the volume flux entering the ice shelf cavity Q_c. The volume fluxes are calculated as

$$Q_g = \int_0^{y_{max}} \int_{-h_b}^{\eta} u|_{x=x_g}\, dz\, dy, \tag{10}$$

$$Q_c = \int_0^{y_{max}} \int_{-h_b}^{\eta - h_0} u|_{x=0}\, dz\, dy, \quad \text{and} \tag{11}$$

$$Q_b = \int_{x_g}^0 \int_{-h_b}^{\eta} v|_{y=0}\, dz\, dx, \tag{12}$$

where x_g is the x location of the center of a gyre that appears in front of the ice shelf (Fig. 3a), and y_{max} is the domain boundary in y direction. From continuity it follows that $Q_C = Q_g + Q_b$. Within the closed volume limited by $x = (x_g, 0)$ and $y = (0, y_{max})$, we additionally calculate the vertical volume

TABLE 2. List of experiments. Note that the viscosity and the Burger number appear in parentheses.

Model run	Grid size dx, dy (m) (viscosity A_h) (m^2 s^{-1})	Time step dt (s)	Ice front width W (km)	Ice draft at front h_0 (m)	Stratification N ($\times 10^{-3}$ s^{-1}) (Bu)	Velocity v_0 (m s^{-1})	Melting
run01 (CTRL)	500 (25)	120	0	300	0	0.1	no
run02	100 (5)	30	0	300	0	0.1	no
run03	250 (12.5)	60	0	300	0	0.1	no
run04	1000 (50)	240	0	300	0	0.1	no
run05	2000 (100)	480	0	300	0	0.1	no
run06	500 (25)	120	0	0	0	0.1	no
run07	500 (25)	120	0	100	0	0.1	no
run08	500 (25)	120	0	200	0	0.1	no
run09	500 (25)	120	0	400	0	0.1	no
run10	500 (25)	120	0	650	0	0.1	no
run11	500 (25)	120	5	300	0	0.1	no
run12	500 (25)	120	10	300	0	0.1	no
run13	500 (25)	120	0	300	0.5 (0.0)	0.1	no
run14	500 (25)	120	0	300	1.7 (0.5)	0.1	no
run15	500 (25)	120	0	300	2.4 (0.9)	0.1	no
run16	500 (25)	120	0	300	3.0 (1.4)	0.1	no
run17	500 (25)	120	0	300	3.4 (1.8)	0.1	no
run18	500 (25)	120	0	300	0	0	yes
run19	500 (25)	120	0	300	0	0.1	yes
run20	500 (25)	120	0	300	2.4 (0.9)	0	yes
run21	500 (25)	120	0	300	2.4 (0.9)	0.1	yes

flux Q_s at the depth of the ice front base $z = -h_0$ to quantify the vertical volume transport (subduction) near the ice front:

$$Q_s = \int_0^{y_{max}} \int_{x_g}^0 w|_{z=-h_0}\, dx\, dy. \tag{13}$$

3. Flow across an ice front: Homogeneous ocean

a. General characteristics of the circulation

The barotropic flow forced at the domain boundaries sets up a geostrophic current along the shelf break (Fig. 3a). The current follows the curvature of the topography into the channel and flows toward the ice shelf along the sloping side of the channel. The curvature of the topography has a large enough radius for the flow to stay attached to the topography (Williams et al. 2001). The volume transport approaching the ice shelf ($Q_g = 0.98$ Sv) (1 Sv $\equiv 10^6$ m^3 s^{-1}) is strongly reduced at the ice front. Only about 25% of the flow enters the ice shelf cavity ($Q_c = 0.25$ Sv), while 75% of the flow is deflected to the right ($Q_b = -0.75$ Sv); that is, most of the flow is blocked by the ice front. The blocked flow creates a strong current of up to 0.17 m s^{-1} parallel to the ice front (Fig. 3f) and feeds the return flow at the opposite side of the channel. A gyre develops in front of the ice shelf with the center x_g located in 45-km distance from the ice front (Fig. 3a). Despite the symmetry of the setup, the circulation in the channel is not fully symmetric, with the core of the return flow shifted toward positive y direction. The flow inside the cavity is steered by the topography of the channel and the sloping base

of the ice shelf to flow along f/H contours (Figs. 2b and 3a) toward the grounding line and back out on the opposite side of the channel where it merges with the return flow.

As the current approaches the ice front, the u velocities decrease from 0.07 m s^{-1} at x_g to 0.029 m s^{-1} at $x = -0.5$ km (Fig. 3b) due to the presence of the ice front that forces the flow to turn to the right. The majority of the flow continues along the ice front as a strong current (Figs. 3a,f). The upper part of the flow that converges at the ice front subducts and reaches high vertical velocities of up to $w = -0.016$ m s^{-1} at $z = -h_0$ (Fig. 3c). These high vertical velocities correspond to 55% of the u velocities at $x = -0.5$ km, which is in approximate agreement with the kinematic boundary conditions (9) and, thus, a consequence of the large topographic step at the ice front. As the whole water column squeezes into the cavity, the flow accelerates horizontally to $u = 0.075$ m s^{-1} and is no longer depth independent but has a maximum at 380-m depth (Figs. 3b,d). The high horizontal velocities only persist about 10 km inside the cavity, where the u velocities are already reduced to 0.013 m s^{-1}, and the v velocities are negligible (Figs. 3b,f). Along the ice front, where a strong current flows in the negative y direction, bottom drag induces an Ekman transport out of the cavity (negative u velocities) within the approximately 15 m thick bottom boundary layer (Figs. 3b,d). This Ekman transport is opposed to the barotropic current at the inflow but aligns with the barotropic current at the outflow. A comparison of experiments with free-slip and no-slip conditions at the vertical faces shows that the circulation is less symmetric at the ice front in the case of no-slip conditions relative to free-slip conditions and that velocities are reduced in
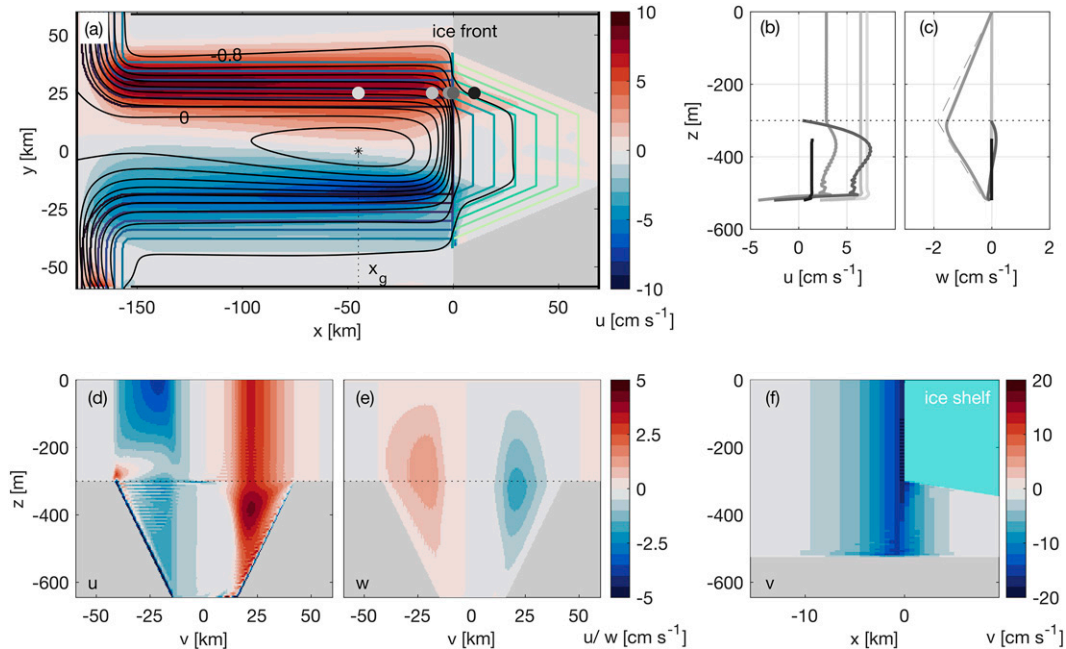
FIG. 3. Steady-state velocities of the CTRL. (a) The depth-averaged u velocity (color) is overlaid by the barotropic streamfunction (black contours) with a transport of 0.1 Sv between the streamlines. Colored contours are lines of constant H (see Fig. 2b). The location of the gyre center at $x = x_g$ is marked with a black dot. Gray-colored circles at distances of $x = -45$ (x_g), -10, -0.5, 0, and 10 km from the ice front show the locations of velocity depth profiles for (b) u and (c) w velocities. The dashed line in (c) shows the theoretical w velocity at the ice front calculated with (9). Also shown are cross sections of (d) u and (e) w velocities at the ice front ($x = -0.5$ km) and (f) v velocity at $y = 25$ km. Grounded ice and bed topography are shaded in gray in (a) and (d)–(f), and the ice shelf is shaded in cyan in (f).

the vicinity of the ice front (not shown). However, the qualitative results and the quantification of the relative volume fluxes compare well.

b. Vorticity dynamics at the ice front

Where the ice shelf intrudes into the ocean, the water column thickness is substantially reduced. Flow that reaches into the cavity is expected to gain positive relative vorticity to conserve PV. Similar idealized studies with a flat bottom and a step topography, show the development of a positive vorticity cell covering the entire shallower region (Tenreiro et al. 2010). Our setup, however, has a sloping bed topography that allows a few f/H contours—notably those for which $H \leq 350$ m—to continue inside the cavity and largely determine the pathway of the flow (Fig. 2b).

The current approaching the ice shelf is geostrophic, indicated by the alignment of the streamlines with f/H contours (Figs. 3a and 4a). For the flow to follow the f/H contours into the cavity, it has to turn sharply right at the ice front and then sharply left to enter the cavity. The flow consequently has negative relative vorticity, ζ, in front of the ice shelf and positive relative vorticity inside the cavity for the part of the flow that enters (Fig. 4b). The flow deviates from f/H contours within about 10 km from the front, but roughly aligns with f/H contours deeper inside the cavity again. Similarly at the outflow, the f/H contours turn left and then right again, creating

positive and negative vorticity, respectively. Ageostrophic motion dominates locally in the vicinity of the ice front, whereas geostrophy governs the flow farther away.

When the flow squeezes underneath the ice shelf, the generation of positive relative vorticity partly balances the step change in water column thickness. Although this aids conservation of PV, Fig. 4c shows that the barotropic streamlines do not align with lines of constant PV across the ice front, which means that PV is not conserved. In the homogeneous system, any changes in PV along a streamline are caused by friction induced by the quadratic drag and viscosity (6). When friction acts as a PV sink, the flow moves toward a smaller (more negative) value of f/H, or, when f is constant, toward smaller isobaths. On the contrary, when friction acts as a PV source, the flow moves toward a larger (less negative) value of f/H, that is, larger isobaths. When PV is conserved while the flow moves toward a different value of f/H, the shift is due to a change in ζ/H.

To illustrate the vorticity changes across the ice front, Figs. 4d–f show the evolution of PV and f/H along three different streamlines ($\Psi_1 = -0.4$ Sv, $\Psi_2 = -0.7$ Sv, $\Psi_3 = -0.78$ Sv) marked in Figs. 4a–c. Streamline Ψ_1 does not enter the cavity, but streamlines Ψ_2 and Ψ_3 do enter. The flow along each of the streamlines can be described as follows:

(i) The flow along the streamline Ψ_1 does not enter the cavity. As the flow is deflected at the ice front, it moves toward larger f/H, i.e., toward larger isobaths (Fig. 4d).

The flow leaving the cavity follows a larger isobath than the flow toward the ice front. PV is increased and friction acts as a PV source along this streamline.

(ii) The flow along the streamline Ψ_2 approaches the ice shelf along a blocked f/H contour, but the flow enters about 4 km into the cavity. The flow arrives on a smaller f/H inside the cavity relative to its initial contour (Fig. 4e), but the PV does not change significantly across the ice front. This means that the decrease in f/H is compensated by an increase in ζ/H and that friction plays a minor role. As the flow exits the cavity, there is a strong dip in PV before the flow eventually flows away from the ice front with a PV value that is larger than in the initial flow toward the ice front. Friction is consequently a net source of PV along this streamline.

(iii) The flow along the streamline Ψ_3 follows an f/H contour that turns sharply at the ice front and continues inside the cavity closer to the center of the channel. The flow shifts to a lower value of f/H (smaller isobath) inside the cavity, thus it moves closer to the grounding line than expected from its f/H contour (Fig. 4f). The PV decreases across the ice front, i.e., friction acts as a PV sink. When the flow exits the cavity, the PV increases again, and friction is a net source of PV.

Strong gradients that occur across the ice front cause a peak and an abrupt step change in the vorticity locally at the ice front. When the streamlines Ψ_2 and Ψ_3 approach the ice shelf, both their PV and f/H increase and peak at the ice front, before being abruptly reduced as soon as the flow crosses the topographic step (Figs. 4e,f). While the changes in f/H are approximately symmetric for the inflow and outflow, the PV has a positive peak at the inflow and a negative peak at the outflow.

To sum up, potential vorticity is not conserved along the streamlines close to the ice front. In total, friction is a PV source, and there is an overall increase in PV between the inflow and the outflow, which means that the outflow is shifted toward deeper water (larger H). However, at the inflow, friction is a PV sink, which allows the flow that enters the cavity to reach closer toward the grounding line (smaller H). Relative vorticity is generated when parts of the flow squeeze into the cavity, and it contributes to the PV budget in the vicinity of the ice front.

4. Sensitivity to resolution and geometry

a. Impact of resolution

We compare the potential vorticity changes along the streamlines Ψ_2 and Ψ_3 for model simulations with different horizontal resolution (Fig. 5) by presenting the PV change into the cavity (from $x = -30$ km at the inflow to the crossing point with $y = 0$) (Figs. 5a,c) and out of the cavity (from the crossing point with $y = 0$ to $x = -30$ km at the outflow) (Figs. 5b,d). In general, the change in PV across the ice front is larger for low-resolution runs (larger grid size); this is because unresolved small-scale motions are parameterized through an increased eddy viscosity parameter at low resolution.

For the flow along Ψ_3, the PV decreases at the inflow and increases at the outflow, as shown in Fig. 4f. For lower

resolution (larger grid size) both the PV sink at the inflow and the PV source at the outflow increase (Figs. 5c,d), and the net effect of resolution on the PV is small. However, because of the increased PV sink at the inflow when using low resolution, the flow reaches deeper into the cavity and closer to the grounding line (smaller f/H and shallower water).

The change in PV along Ψ_2 is less symmetric at the inflow and outflow (Figs. 5a,b). While the PV is conserved at the inflow for any resolution, the PV increases at the outflow for low resolution; the return flow is shifted toward larger isobaths (larger f/H). For high resolution, relative vorticity is generated and ζ/H changes along the streamline: ζ/H increases at the inflow, moving the streamline toward smaller f/H contours, and it decreases again at the outflow, to conserve PV (Figs. 5c,d). Although the streamline Ψ_2 lies on an f/H contour that does not continue inside the cavity, the flow enters the cavity under the generation of positive relative vorticity (Fig. 4).

b. Impact of ice shelf thickness and ice front steepness

The thickness of ice fronts around Antarctica ranges from 50 to 400 m (Liu et al. 2015) and varies in time due to ice shelf mass loss and gain. Here, we investigate how the thickness of the ice shelf affects the fraction of the barotropic flow that enters the cavity.

The volume flux into the cavity Q_c decreases with an increased ice shelf draft (Fig. 6a). However, in all cases, the modeled volume flux exceeds the flux expected to enter the cavity if the flow was following f/H contours. This excess volume flux increases for an increased ice shelf draft. For an ice shelf draft with $h_0 = 400$ m, there are no f/H contours that continue into the cavity, but the modeled flux across the ice front is about $Q_c = 0.13$ Sv (13% of Q_g) because of ageostrophic motion. Inside the cavity, the volume flux is expected to decrease approximately linearly with distance from the ice front (Fig. 6c). For small ice shelf drafts (≤ 100 m), the volume flux indeed decreases approximately linearly toward the grounding zone; for a larger ice shelf draft (≥ 200 m), however, the decrease is nonlinear and does not correspond to the changes in water column thickness. In those cases, the volume flux is higher than expected from f/H contours within the first 10 km of the cavity, but it decreases rapidly with distance from the front.

As seen in Fig. 3c, the convergence at the ice front causes high vertical velocities. The subduction Q_s at the ice front increases with increased ice shelf draft and decreases again for very thick ice shelves (Fig. 6b). The increasing vertical velocities are a result of the increased ice shelf draft (9), and the decrease with even larger drafts is due to a reduction in horizontal velocities at the ice front, as more water is deflected at greater distance from the ice front.

Despite a generally reduced volume flux into the cavity for increased ice shelf draft, a thicker ice shelf causes higher velocities along the ice front and at the first kilometers within the ice shelf cavity (Figs. 6d,e). For a thinner ice shelf, velocities at the ice front are generally smaller, but the flow reaches deeper into the cavity. Thus, the flow speeds up more as the water column squeezes through a smaller
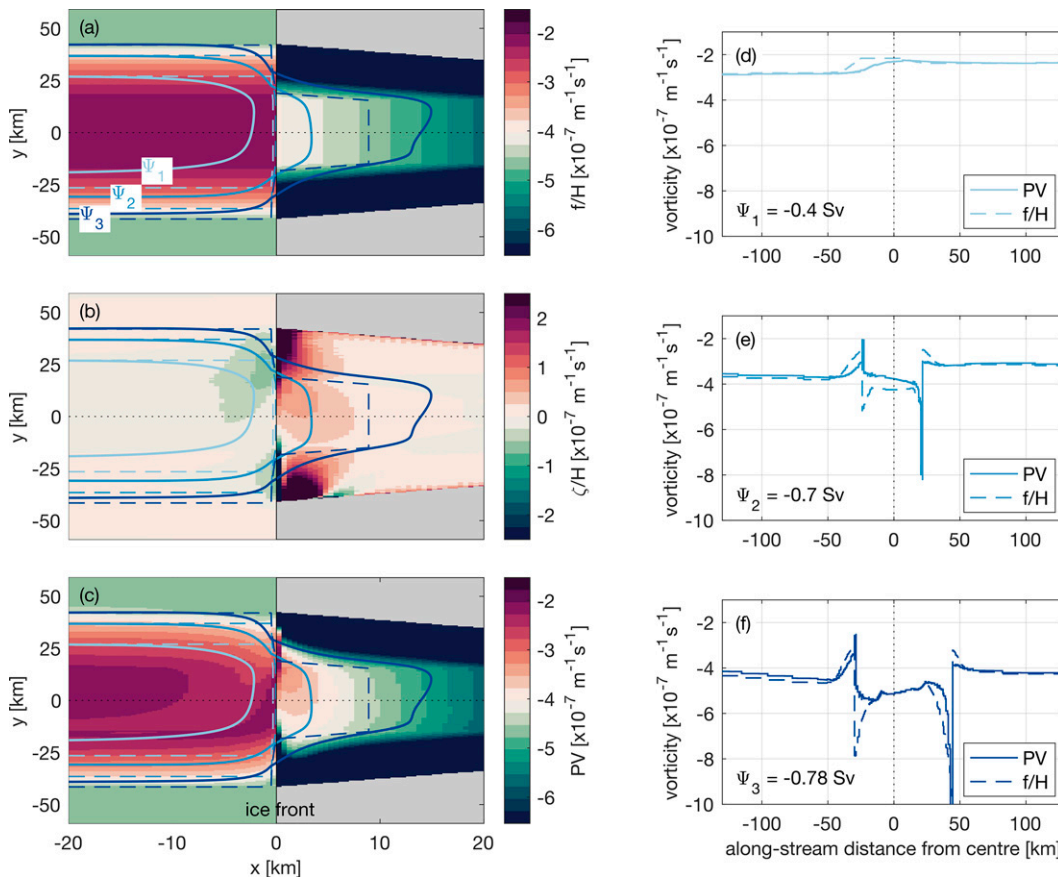
FIG. 4. Potential vorticity for the CTRL divided into (a) f/H, (b) ζ/H, and (c) PV $= (f + \zeta)/H$. Blue contours in (a)–(c) mark three streamlines $\Psi_1 = -0.4$ Sv, $\Psi_2 = -0.7$ Sv, and $\Psi_3 = -0.78$ Sv (solid) and the corresponding f/H contours that they are following at the inflow (dashed). The dotted black line at $y = 0$ marks the center line. Also shown are PV and f/H along the three streamlines (d) Ψ_1, (e) Ψ_2, and (f) Ψ_3 with along-streamline distance from the crossing point with the center line.

area, and the acceleration is associated with strong subduction (Fig. 6b).

The strength of the topographic barrier at the ice front can also be reduced through tilting the ice front, which increases the width of the ice front W (Fig. 2c). We present the volume flux into the cavity and the PV along streamlines for $W = 0, 5$, and 10 km (Fig. 7). The water column thickness inside the cavity ($x > 0$ km) is the same for all three model simulations, and consequently, the theoretical volume flux based on f/H is the same. However, for smaller W the flow reaches slightly deeper into the cavity (Fig. 7a) and the modeled volume flux is larger within the first 10 km of the cavity (Fig. 7b): In case of the vertical ice front ($W = 0$), 25% (about 0.25 Sv) of Q_g enters the cavity (crosses $x = 0$ km), whereas only 14% enters if $W = 10$ km. A comparison of PV along the streamlines for the three different model simulations shows that PV is better conserved along the streamlines for a more tilted ice front (larger W, Fig. 7c). The f/H contours turn less abruptly when the ice front is tilted, and the flow can follow f/H contours more easily. More gradual changes in f/H contours lead to smaller changes in relative vorticity and reduced frictional effects.

5. Flow across an ice front: Stratified ocean

Now, we investigate the influence of an ambient linear stratification on the externally forced barotropic circulation and the volume fluxes into the ice shelf cavity. We present the circulation for a stratification of $N = 2.4 \times 10^{-3}$ s^{-1}, which corresponds to the stratification measured during summer in Siple Trough at the depth of the ice shelf draft ($-100 < z < -500$ m; Fig. 2d). The circulation (Fig. 8) reveals the following differences in comparison with the homogeneous run: (i) fewer streamlines cross the ice front, (ii) the center of the gyre is located farther away from the ice front ($x_g = -72$ km as compared with $x_g = -45$ km in the homogeneous run; Fig. 8a), (iii) velocities parallel to the ice front are reduced by 40% (Fig. 8f), and iv) maximum vertical velocities are reduced by 80% ($w = -0.002$ vs -0.01 m s^{-1}) so that the flow barely accelerates across the ice front (Figs. 8b–e).

The volume flux entering the cavity decreases with increased stratification, as vertical motion is increasingly suppressed (Fig. 9b), and less water squeezes into the cavity (Fig. 9a). In the case of no stratification ($N = 0$) the volume flux into the cavity Q_c is 25% of Q_g, whereas in the case
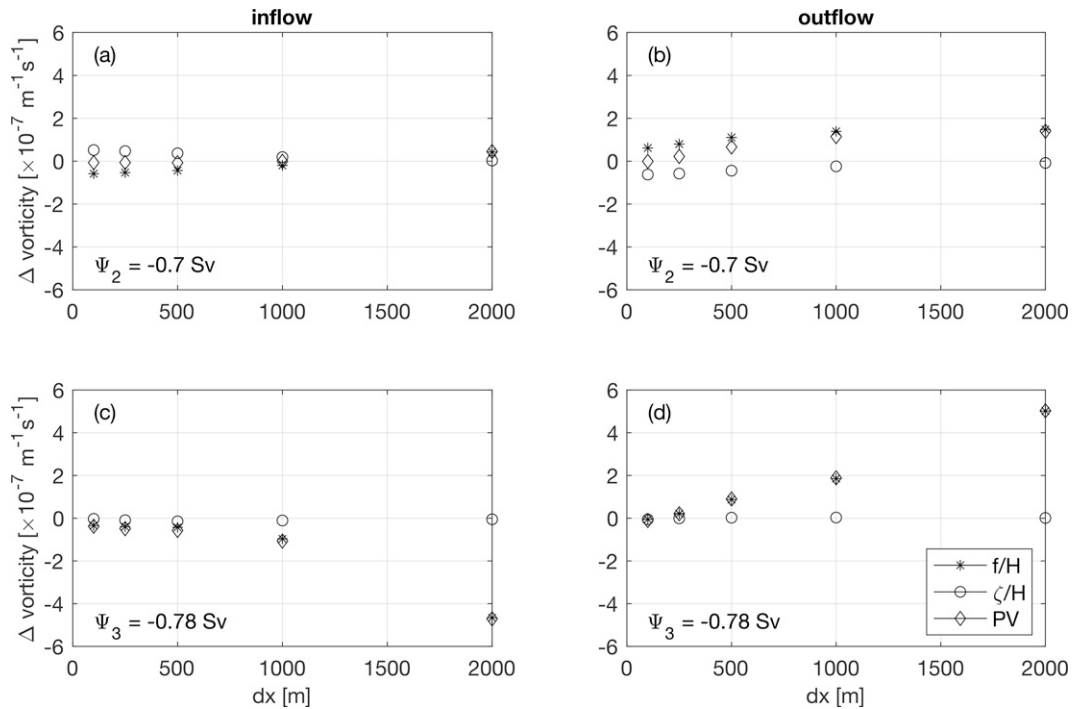
Fig. 5. Comparison of the changes in f/H (asterisks), ζ/H (circles), and PV $= (f + \zeta)/H$ (diamonds) into the cavity and out of the cavity for different model resolutions (run01–run05). The changes are calculated along the streamlines (a),(b) $\Psi_2 = -0.7$ Sv and (c),(d) $\Psi_3 = -0.78$ Sv, showing (left) the differences in vorticity at $y = 0$ km minus the vorticity at $x = -30$ km (inflow) and (right) the difference in vorticity at $x = -30$ km (return flow) minus the vorticity at $y = 0$ km (outflow). Note that the lateral eddy viscosity parameter A_h is adjusted to the resolution (Table 2).

of strong stratification ($N = 3.4 \times 10^{-3}$ s^{-1}) the entering volume flux is only 2% of Q_g (Fig. 9a).

For a stratification of $N = 2.4 \times 10^{-3}$–3.0×10^{-3} s^{-1} (Bu ≈ 1), depth-varying vertical velocities at the ice front induce a downward tilt in isopycnals toward the ice front and hence vertical shear (Figs. 8c,f). An anticyclonic baroclinic circulation associated with the tilting isopycnals is superimposed on the cyclonic, barotropic circulation, leading to negative volume fluxes inside the cavity (Fig. 9c). If the stratification is strong ($N = 3.4 \times 10^{-3}$ s^{-1}; Bu $= 1.8$), vertical velocities are restrained, reducing the tilt in isopycnals and leading to small velocities inside the cavity.

6. Implications for ice shelf melt

So far, this study has focused on the dynamics across the ice front and the volume fluxes entering the cavity. But to what extent does the externally driven barotropic circulation affect melt rates at the ice shelf base? Basal melt rates are determined by the conductive heat into the ice and the turbulent heat flux through the ice–ocean boundary layer (Jenkins et al. 2010). The latter is a function of the turbulence intensity controlled by the current velocity below the boundary layer. The strength of the circulation also determines the transport of heat into and advection of meltwater out of the cavity. The velocity inside the cavity consequently not only determines how oceanic heat is distributed, but also the efficiency of the heat transfer toward the ice base. Here,

we compare modeled melt rates from simulations with and without an externally forced barotropic flow (Fig. 10).

The purely melt-driven circulation is characterized by a geostrophic cross-slope current parallel to the sloping base of the ice shelf (Fig. 10a), which is typical for the gently sloping ice shelves of Antarctica (Jenkins et al. 2016). Melt rates are almost constant in the interior of the ice shelf cavity and about 2 times as high along the boundary where the meltwater converges and exits the cavity as a buoyant plume.

When we add an externally forced barotropic current, the melt rates increase in the frontal region, where a lateral boundary current develops (Fig. 10b). The melt rates reflect the strength of the current, and we expect increased melt in the frontal region when the ice shelf is thick, and increased melt rates deeper into the cavity when the ice shelf is thin (Figs. 6d–f). In the model simulations shown here, the thermal driving is $\Theta - \Theta_f = 1.9°$C and the relative contribution of the externally driven barotropic flow on total melt rates is 11% in comparison with the melt-only case. This relative contribution increases with decreasing ocean temperature. The contribution of the barotropic flow to total melt rates is 26% for $\Theta = -1$, where the thermal driving is reduced to $\Theta - \Theta_f = 0.9°$C (not shown here).

In a linearly stratified ocean, the effect of an externally forced barotropic flow on basal melt rates is smaller than it is in the homogeneous case (Fig. 10c). This is related to the reduced volume flux entering the cavity. However, we only
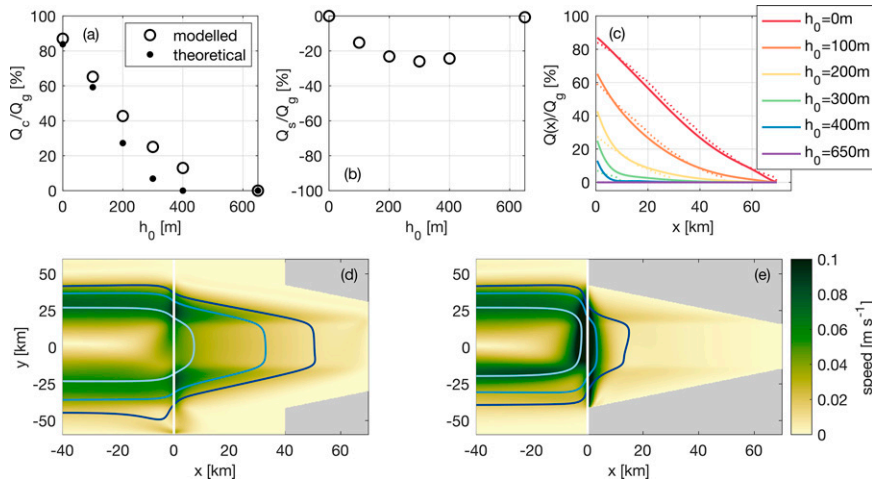
FIG. 6. Volume fluxes (10)–(13) and current speed for different ice shelf drafts $h_0 = 0$–650 m (run01 and run06–run10). (a) Flux into the cavity Q_c (at $x = 0$) relative to the approaching flux Q_g (at the center of the gyre at $x = x_g$); (b) vertical flux in front of the ice shelf Q_s (at $z = h_0$) relative to Q_g; (c) flux into the cavity relative to Q_g as a function of x. Small dots in (a) and dashed lines in (c) correspond to the flux if the current at Q_g was geostrophic, i.e., following f/H contours. Also shown is the speed of the depth-averaged current overlaid by the three streamlines Ψ_1, Ψ_2, and Ψ_3 (blue contours) for ice shelf drafts with (d) $h_0 = 100$ m (run07) and (e) $h_0 = 300$ m (CTRL and run01).

consider stratification in salinity and do not include any vertical variability in temperature. In an ocean with depth-varying temperature, the temperature of the water that reaches the ice shelf base has to be considered.

7. Discussion

In this study, we use an idealized numerical model to explore the blocking effect of an ice front on an externally forced barotropic current; a phenomenon that has previously been observed at the Getz Ice Shelf in West Antarctica (Wåhlin et al. 2020). We show that stratification and ice shelf thickness determine the fraction of the barotropic current that enters the ice shelf cavity. When the barotropic current enters the cavity in a homogeneous ocean, ageostrophic processes and subduction become important in the vicinity of the ice front.

The idealized model simulations of a barotropic flow approaching an ice shelf reproduce the observations from laboratory experiments with a similar setup presented in Wåhlin et al. (2020). The externally forced barotropic current follows the sloping side of the channel and bifurcates at the ice front; the majority of the flow is deflected to the right to follow the topographic step of the ice front with the shallower water to its left (Southern Hemisphere), while a smaller fraction (25% of the approaching volume transport in the control run) enters the cavity. In comparison with the laboratory experiments (Wåhlin et al. 2020), the reduction in u velocities (toward the ice shelf) across the topographic step is similar (Fig. 3b): the velocities are reduced by 82% in the control simulation (46% reduction of the water column thickness at the ice front) and by 72% in the laboratory (36% reduction of the water column thickness).
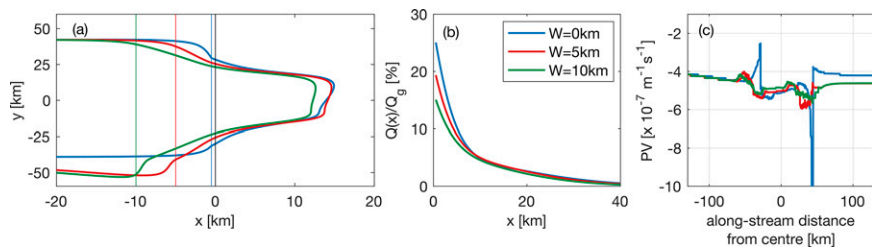

FIG. 7. Results from model simulations with tilted ice front (run01, run11, and run12). (a) Streamline $\Psi_1 = -0.78$ Sv for $W = 0$ (blue), $W = 5$ km (red), and $W = 10$ km (green). The black line at $x = 0$ marks the ice front at the base, and the colored lines mark the ice front at the surface for each model run. (b) Volume flux into the cavity relative to Q_g as a function of x. (c) The PV along Ψ_1 with along-streamline distance from the crossing point with the center line for the three model runs.
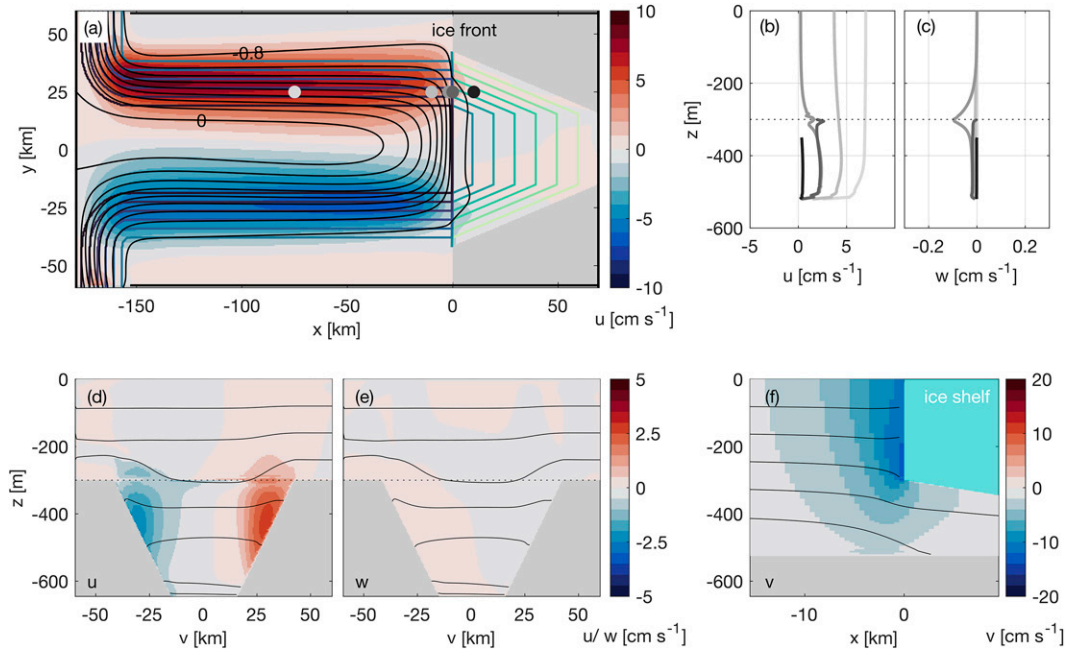
FIG. 8. As in Fig. 3, with linear stratification ($N = 2.4 \times 10^{-3}$ s^{-1}; run15). (a) The depth-averaged u velocity (color) is overlaid by the barotropic streamfunction (black contours) with a transport of 0.1 Sv between the streamlines. Colored contours mark lines of constant H (see Fig. 2b). Gray-colored circles at distances of $x = -45$ (x_g), -10, -0.5, 0, and 10 km from the ice front show the locations of velocity depth profiles for (b) u and (c) w velocities. Also shown are cross sections of (d) u and (e) w velocities at the ice front ($x = -0.5$ km) and (f) v velocity at $y = 25$ km. Black contours in (d)–(f) mark isopycnals. Gray shading in (a) and (d)–(f) is grounded ice and bed topography, respectively, and the cyan box in (f) is the ice shelf.

We showed that the part of the flow entering the ice shelf cavity crosses the topographic step at the ice front due to the continuation of a few f/H contours into the cavity and due to frictional processes. The volume transport into the ice shelf cavity is to a large degree determined by the thickness of the ice shelf, i.e., the size of the topographic step. The part of the flow that enters the ice shelf cavity approaches the grounding line, turns right, and exits the cavity at the opposite side—a pathway that is mainly dictated by the lines of constant water column thickness given by the geometry of the channel and the ice shelf base. The flow into and out of the cavity is asymmetric, despite the symmetric geometry. This asymmetry between the inflow and the outflow and the simulated bifurcation of the inflowing current at the ice front agrees with the

findings by Carnevale et al. (1999) and Sansón et al. (2005), who found a different dynamical behavior of a coastal current encountering a topographic step depending on whether the topography is shoaling or deepening relative to the coast. Although in our setting the current is not a coastal current and the topographic step is induced by the ice shelf, i.e., from the surface rather than from the bottom, the framework by Carnevale et al. (1999) can be used to explain the asymmetry: The flow into the cavity may be considered as the Southern Hemisphere equivalent for their right-handed, step-up flow that either deflects entirely or bifurcates at the escarpment with the development of a current along the step away from the coast—in our case the blocked current along the ice front. The flow out of the cavity would be the Southern
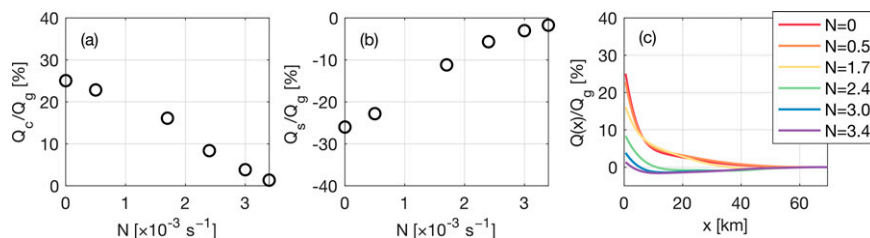

FIG. 9. Volume fluxes (10)–(13) for runs with different stratification N ($\times 10^{-3}$ s^{-1}) (run01 and run13–run17). (a) Flux into the cavity Q_c (at $x = 0$) relative to the approaching flux Q_g (at the center of the gyre at $x = x_g$); (b) vertical flux in front of the ice shelf Q_s (at $z = -h_0$) relative to Q_g; (c) flux into the cavity relative to Q_g as a function of x.
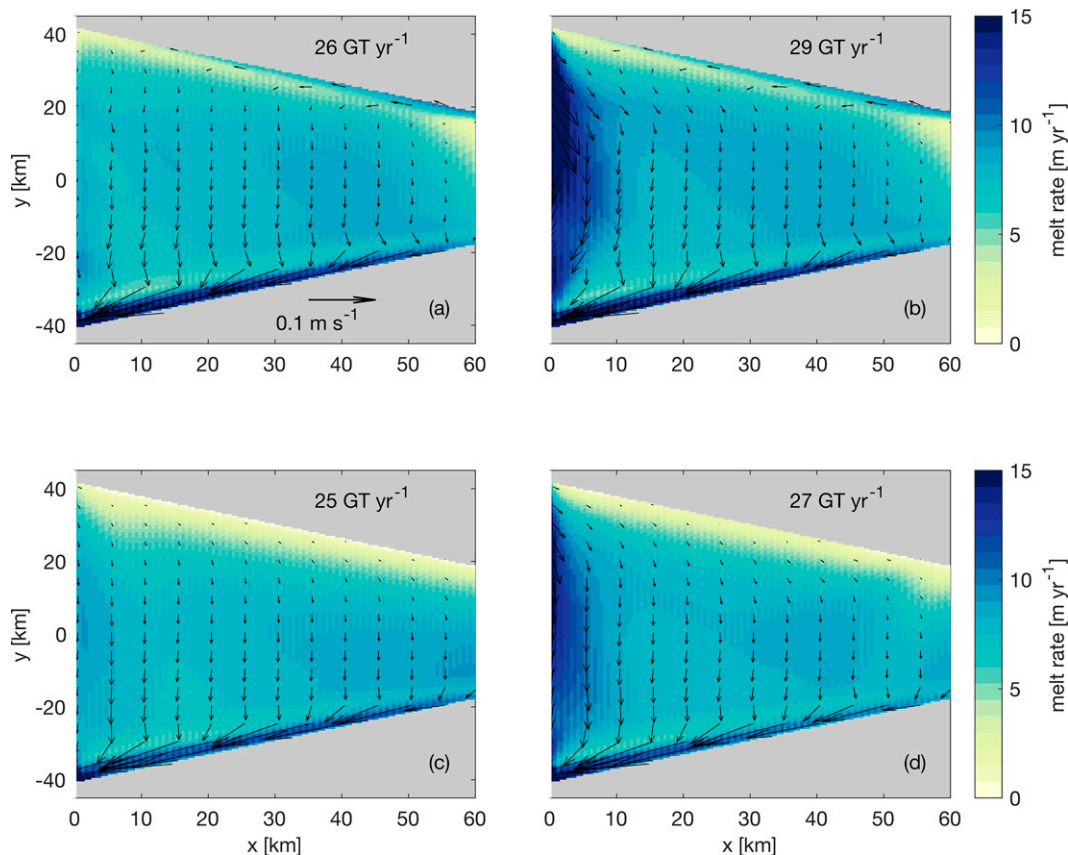
FIG. 10. Melt rates and mean velocities in the uppermost 20 m of the water column for model simulations with basal melting turned on. (a),(b) Initially homogeneous (run18–19) and (c),(d) initially linearly stratified in salinity with $N = 2.4 \times 10^{-3}$ s^{-1} (run20 and run21). In (a) and (c) the circulation is only driven by basal melting, whereas in (b) and (d) the circulation is driven by basal melting and an externally forced barotropic current.

Hemisphere equivalent for their left-handed, step-down flow, which speeds up as it merges with the "onshore" current along the step when crossing the step into deeper waters. Asymmetry is in addition induced by the changes in the PV along the pathway of the current (Fig. 4).

The model results show that in the homogeneous case geostrophy determines the circulation pattern and the volume flux entering the cavity to a first approximation and beyond about 10 km from the ice front. Closer to the ice front, ageostrophic processes play a large role in squeezing parts of the flow into the cavity. While the streamlines deviate from their f/H contours locally at the ice front, the volume flux into the cavity is strongly dependent on the ice shelf thickness and the bed topography (Fig. 6). Accurate measurements of the bathymetry and ice thickness are consequently necessary to predict heat fluxes into the cavity and consequent basal melt rates.

A comparison of PV along streamlines for different model resolutions (section 4a) reveals that PV is less conserved in the frontal region in lower-resolution models that compensate unresolved small-scale processes with high eddy viscosity. The effect of resolution on the modeled flow is twofold: on one hand, less water enters the cavity in low-resolution models, as they cannot resolve small-scale processes that help the flow to

cross the ice front. On the other hand, water that does enter the cavity can move closer to the grounding line due to a stronger decrease in PV across the ice front. Consequently, the total effect of reduced resolution on basal melt rates is unclear. Melt rates at the ice front are likely underestimated in low-resolution models, while melt rates close to the grounding zone might be overestimated. Previous studies have shown that a resolution of less than 1 km is needed to adequately capture eddies and ageostrophic processes that allow the flow to cross geostrophic contours (Årthun et al. 2013; St-Laurent et al. 2013; Stewart and Thompson 2015).

Our model simulations show high velocities and enhanced basal melting in a 10-km-wide boundary zone along the ice front (section 6). The thermal forcing is typically largest near the deep grounding zone, inducing high basal melt rates there, but the velocity dependency of the turbulent transfer coefficients shifts the melt pattern toward regions of high velocities at the ice–ocean interface (Dansereau et al. 2014). The relative contribution of velocity-driven basal melting versus thermal melting is expected to play a larger role for cold cavities (section 6). Satellite-based estimates of basal melt rates show strong melting in the frontal zone of the Ross Ice Shelf and the Filchner–Ronne Ice Shelf (Moholdt et al. 2014). The melt rates

at the Ross Ice Shelf have been associated with seasonal inflow of relatively warm surface water during summer (Stewart et al. 2019) and increased velocities at the ice front due to tides and plume dynamics (Horgan et al. 2011). High melt rates at the front of the Filchner–Ronne Ice shelf might be linked to strong tidal currents that flow parallel to the ice front (Padman et al. 2018). Generally, basal melting at the ice front is expected to have a small influence on the stability of the ice shelf, unless it influences calving rates of ice shelves that are in imbalance, such as in the Amundsen Sea (Fürst et al. 2016). Nevertheless, enhanced melting in the frontal region increases meltwater production and has been suggested to increase the inflow of surface waters into the cavity through a wedge mechanism induced by a modified stratification (Malyarenko et al. 2019).

The stratified model simulations (section 5) show that the volume flux into the cavity decreases with increased stratification, due to suppressed vertical velocities in front of the ice shelf. Among the different linear stratification profiles explored in this study, a stratification of $N = 2.4 \times 10^{-3}$ s^{-1} (Fig. 8) corresponds best to the summer observations at the Getz Ice Shelf at middepth. Scaling analysis gives a Burger number of about 1, which suggests that the flow is approximately equally influenced by rotation and stratification. Homogenization of the upper water column through, for example, wintertime convection would decrease the Burger number. This would strengthen the boundary current along the ice front and increase the vertical velocities at the ice front. Events of strong barotropic, along-ice front currents and a deepened, homogeneous surface layer extending toward the bottom have been observed at the Getz Ice Shelf front during strong wind events (Steiger et al. 2021). Increased stratification, in turn, would strengthen the blocking of the barotropic current at the ice front.

Basal melt rates are strongly influenced by the temperature profile of the water mass entering the cavity, in addition to volume fluxes considered in this study (Jenkins 1991; Holland et al. 2008). In continental shelf regions where warm water occupies the lower part of the water column (such as the Amundsen Sea), the base of the ice shelf is directly exposed to the higher temperatures. The flow of warm water toward the cavity is typically bottom enhanced; that is, the flow has a baroclinic component that can enter the ice shelf cavity freely and a barotropic component that would be at least partly blocked (Wåhlin et al. 2020). In cold continental shelf regions, basal melting can result from the inflow of seasonally warm surface waters, described by Jacobs et al. (1992) as basal melting mode III. Our model simulations with no/weak stratification suggest subduction of the upper part of the water column, which might enhance the inflow of surface waters and modify the properties of the inflowing water. The homogeneous simulations presented here would be representative for winter conditions on a cold shelf, as the water column tends to be homogenized following surface cooling and sea ice formation. Dense water formation in ice front polynyas—observed, for example, at the Ronne Ice Front in the Weddell Sea—produces density fronts and (frontal instabilities) eddies that contribute significantly to the cross-front exchange (Årthun et al. 2013).

8. Conclusions

This idealized modeling study explores the dynamics of an externally forced barotropic flow that approaches an ice front along the sloping side of a channel incised into the continental shelf. We investigate the potential vorticity budget in the vicinity of the ice front and quantify the volume flux entering the ice shelf cavity for different ice shelf thicknesses and (linear) ocean stratification.

We find that the barotropic flow to a good approximation follows lines of constant f/H. Thus, the flow approaches the ice front along the sloping side of the channel and returns toward the shelf break along the opposite side of the channel. The ice front represents an abrupt change in water column thickness, H, but a limited number of f/H contours continue into the ice shelf cavity, due to the sloping sides of the channel. The number of f/H contours that continue into the ice shelf cavity is smaller the larger the ice shelf thickness. Typically, the majority of f/H contours do not continue into the cavity and, as a consequence, a large fraction of the barotropic flow cannot enter the cavity. Instead, the flow is deflected at the ice front and continues as a narrow boundary current along the ice front that joins the return flow on the opposite side of the channel.

In the proximity of the ice front, where f/H contours change direction sharply to collapse along the ice front, the flow deviates from f/H contours under the influence of ageostrophic processes. The fraction of the flow that enters the cavity gains positive relative vorticity due to the squeezing of the water column. The squeezing is associated with vertical velocities (subduction) in front of the ice shelf and high horizontal velocities parallel to the ice front within the first kilometers of the cavity, more so for thicker ice shelves than for thinner ones. The subduction is greatly reduced when the ocean is linearly stratified, and the volume flux entering the cavity is consequently reduced.

Relative vorticity at the ice front allows the flow to squeeze into the cavity in a well-mixed ocean. Since the gradients increase in the vicinity of the ice front, viscous forces become important and influence the PV budget. Viscosity acts as a PV sink on the way into the cavity and a PV source on the way out of the cavity. The flow consequently follows a shallower f/H contour inside the cavity than outside and can therefore reach deeper into the cavity. This effect is exaggerated in low-resolution model runs, where an increased eddy viscosity parameter is used to account for unresolved small-scale motion. In the vicinity of the ice front where a strong current flows along the ice front, drag at the seafloor and the ice shelf base induces a boundary flow directed out of the cavity.

The externally forced barotropic flow increases melt rates in the frontal region, where the strong lateral flow undercuts the ice front. This effect is stronger when the stratification is weak and the ice shelf is thick. These melt rates occur in addition to the melting that is induced by the melt-driven circulation inside the cavity. The amount of blocking by the ice front is consequently of importance for the basal melting both due to the heat transported by the barotropic flow toward the ice shelf base and the high velocities induced at the front.

APPENDIX

Derivation of the Barotropic Potential Vorticity Equation in a Homogeneous Ocean

The barotropic potential vorticity equation originates from the curl of the depth-integrated momentum equation in (1) divided by H (Hughes 2008). Because we are interested in the barotropic flow, we integrate over depth the equations for the homogeneous case from the bottom $(-h_b)$ to the surface $(\eta - h_{is})$. To account for vertical shear that occurs at the ice front and along the topography, we split the velocity into the vertical mean $\overline{\mathbf{u}}$ and the deviation from the vertical mean $\tilde{\mathbf{u}}$ in analogy to Reynolds averaging such that $\mathbf{u} = \overline{\mathbf{u}} + \tilde{\mathbf{u}}$ (Özsoy 2020). The depth integration of the Lagrangian derivative then results in

$$\int_{-h_b}^{\eta-h_{is}} \frac{D\mathbf{u}}{Dt}\, dz = H\frac{D\overline{\mathbf{u}}}{Dt} + \frac{\partial}{\partial x}H\overline{\tilde{u}\tilde{\mathbf{u}}} + \frac{\partial}{\partial y}H\overline{\tilde{v}\tilde{\mathbf{u}}}. \tag{A1}$$

The last two terms are the dispersive momentum transport that describes exchange processes due to vertical nonuniformity and can be combined with the frictional terms. In this setup, the forcing is barotropic and density is constant, such that vertical shear can only occur through friction.

The resulting barotropic potential vorticity equation can then be rearranged to

$$\frac{D}{Dt}\left(\frac{f+\zeta}{H}\right) = \frac{1}{H}\mathbf{k} \cdot \nabla \times \left[\frac{\boldsymbol{\tau}_s - \boldsymbol{\tau}_b}{H} + \frac{1}{H}\int_{-h_b}^{\eta-h_{is}}(A_h\nabla_h^2\mathbf{u})\,dz \right.$$
$$\left. + \frac{1}{H}\frac{\partial}{\partial x}H\overline{\tilde{u}\tilde{\mathbf{u}}} + \frac{1}{H}\frac{\partial}{\partial y}H\overline{\tilde{v}\tilde{\mathbf{u}}}\right], \tag{A2}$$

where the stress terms at the surface $\boldsymbol{\tau}_s$, that is, at the base of the ice shelf, and at the bottom $\boldsymbol{\tau}_b$ result from the quadratic drag. For barotropic flow, the curl of the pressure

gradient term is zero, and the vertical viscous term [second-to-last term in (1)] vanishes during depth integration. All terms on the right-hand side of (A2) are frictional processes and are combined to one frictional term F in (6). In the stratified runs, baroclinic currents develop in the vicinity of the ice shelf front (because the vertical velocities here cause the isopycnals to tilt), and an additional term, representing baroclinic vorticity generation, must be included in the vorticity budget.

REFERENCES

Adcroft, A., C. Hill, and J. Marshall, 1997: Representation of topography by shaved cells in a height coordinate ocean model. *Mon. Wea. Rev.*, **125**, 2293–2315, https://doi.org/10.1175/1520-0493(1997)125<2293:ROTBSC>2.0.CO;2.

——, and Coauthors, 2018: MITgcm documentation. MITgcm, https://mitgcm.readthedocs.io/en/latest/.

Arneborg, L., A. K. Wåhlin, G. Björk, B. Liljebladh, and A. H. Orsi, 2012: Persistent in-flow of warm water onto the central Amundsen shelf. *Nat. Geosci.*, **5**, 876–880, https://doi.org/10.1038/ngeo1644.

Årthun, M., P. R. Holland, K. W. Nicholls, and D. L. Feltham, 2013: Eddy-driven exchange between the open ocean and a sub–ice shelf cavity. *J. Phys. Oceanogr.*, **43**, 2372–2387, https://doi.org/10.1175/JPO-D-13-0137.1.

Assmann, K. M., E. Darelius, A. Wåhlin, T. W. Kim, and S. H. Lee, 2019: Warm circumpolar deep water at the western Getz Ice Shelf front, Antarctica. *Geophys. Res. Lett.*, **46**, 870–878, https://doi.org/10.1029/2018GL081354.

Carnevale, G. F., S. G. L. Smith, F. Crisciani, R. Purini, and R. Serravall, 1999: Bifurcation of a coastal current at an escarpment. *J. Phys. Oceanogr.*, **29**, 969–985, https://doi.org/10.1175/1520-0485(1999)029<0969:BOACCA>2.0.CO;2.

Cushman-Roisin, B., and J.-M. Beckers, 2011: *Introduction to Geophysical Fluid Dynamics: Physical and Numerical Aspects.* 2nd ed. International Geophysical Series, Vol. 101, Academic Press, 760 pp.

Dansereau, V., P. Heimbach, and M. Losch, 2014: Simulation of subice shelf melt rates in a general circulation model: Velocity-dependent transfer and the role of friction. *J. Geophys. Res. Oceans*, **119**, 1765–1790, https://doi.org/10.1002/2013JC008846.

Determann, J., and R. Gerdes, 1994: Melting and freezing beneath ice shelves: Implications from a three-dimensional ocean-circulation model. *Ann. Glaciol.*, **20**, 413–419, https://doi.org/10.3189/1994AoG20-1-413-419.

Dinniman, M. S., and J. M. Klinck, 2004: A model study of circulation and cross-shelf exchange on the west Antarctic Peninsula continental shelf. *Deep-Sea Res. II*, **51**, 2003–2022, https://doi.org/10.1016/j.dsr2.2004.07.030.

Foldvik, A., T. Gammelsrød, E. Nygaard, and S. Østerhus, 2001: Current measurements near Ronne Ice Shelf: Implications for circulation and melting. *J. Geophys. Res.*, **106**, 4463–4477, https://doi.org/10.1029/2000JC000217.

Fürst, J. J., G. Durand, F. Gillet-Chaulet, L. Tavard, M. Rankl, M. Braun, and O. Gagliardini, 2016: The safety band of Antarctic ice shelves. *Nat. Climate Change*, **6**, 479–482, https://doi.org/10.1038/nclimate2912.

Grosfeld, K., R. Gerdes, and J. Determann, 1997: Thermohaline circulation and interaction between ice shelf cavities and the adjacent open ocean. *J. Geophys. Res.*, **102**, 15 595–15 610, https://doi.org/10.1029/97JC00891.

Ha, H. K., and Coauthors, 2014: Circulation and modification of warm deep water on the central Amundsen Shelf. *J. Phys. Oceanogr.*, **44**, 1493–1501, https://doi.org/10.1175/JPO-D-13-0240.1.

Holland, D. M., and A. Jenkins, 1999: Modeling thermodynamic ice-ocean interactions at the base of an ice shelf. *J. Phys. Oceanogr.*, **29**, 1787–1800, https://doi.org/10.1175/1520-0485(1999)029%3C1787:MTIOIA%3E2.0.CO;2.

Holland, P. R., 2017: The transient response of ice shelf melting to ocean change. *J. Phys. Oceanogr.*, **47**, 2101–2114, https://doi.org/10.1175/JPO-D-17-0071.1.

——, A. Jenkins, and D. M. Holland, 2008: The response of ice shelf basal melting to variations in ocean temperature. *J. Climate*, **21**, 2558–2572, https://doi.org/10.1175/2007JCLI1909.1.

Horgan, H. J., R. T. Walker, S. Anandakrishnan, and R. B. Alley, 2011: Surface elevation changes at the front of the Ross Ice Shelf: Implications for basal melting. *J. Geophys. Res.*, **116**, C02005, https://doi.org/10.1029/2010JC006192.

Hughes, C. W., 2008: A form of potential vorticity equation for depth-integrated flow with a free surface. *J. Phys. Oceanogr.*, **38**, 1131–1136, https://doi.org/10.1175/2007JPO3809.1.

Huneke, W. G. C., A. Klocker, and B. K. Galton-Fenzi, 2019: Deep bottom mixed layer drives intrinsic variability of the Antarctic slope front. *J. Phys. Oceanogr.*, **49**, 3163–3177, https://doi.org/10.1175/JPO-D-19-0044.1.

Jacobs, S. S., H. H. Helmer, C. S. M. Doake, A. Jenkins, and R. M. Frolich, 1992: Melting of ice shelves and the mass balance of Antarctica. *J. Glaciol.*, **38**, 375–387, https://doi.org/10.1017/S0022143000002252.

——, A. Jenkins, H. Hellmer, C. Giulivi, F. Nitsche, B. Huber, and R. Guerrero, 2012: The Amundsen Sea and the Antarctic ice sheet. *Oceanography*, **25**, 154–163, https://doi.org/10.5670/oceanog.2012.90.

Jenkins, A., 1991: A one-dimensional model of ice shelf-ocean interaction. *J. Geophys. Res.*, **96**, 20 671–20 677, https://doi.org/10.1029/91JC01842.

——, H. H. Hellmer, and D. M. Holland, 2001: The role of meltwater advection in the formulation of conservative boundary conditions at an ice–ocean interface. *J. Phys. Oceanogr.*, **31**, 285–296, https://doi.org/10.1175/1520-0485(2001)031%3C0285:TROMAI%3E2.0.CO;2.

——, P. Dutrieux, S. S. Jacobs, S. D. McPhail, J. R. Perrett, A. T. Webb, and D. White, 2010: Observations beneath pine island glacier in West-Antarctica and implications for its retreat. *Nat. Geosci.*, **3**, 468–472, https://doi.org/10.1038/ngeo890.

——, ——, S. Jacobs, E. J. Steig, G. H. Gudmundsson, and J. Smith, 2016: Decadal ocean forcing and Antarctic ice sheet response: Lessons from the Amundsen Sea. *Oceanography*, **29**, 106–117, https://doi.org/10.5670/oceanog.2016.103.

Jourdain, N. C., P. Mathiot, N. Merino, G. Durand, J. Le Sommer, P. Spence, P. Dutrieux, and G. Madec, 2017: Ocean circulation and sea-ice thinning induced by melting ice shelves in the Amundsen Sea. *J. Geophys. Res. Oceans*, **122**, 2550–2573, https://doi.org/10.1002/2016JC012509.

Kalén, O., K. M. Assmann, A. K. Wåhlin, H. K. Ha, T. W. Kim, and S. H. Lee, 2016: Is the oceanic heat flux on the central Amundsen Sea Shelf caused by barotropic or baroclinic currents? *Deep-Sea Res. II*, **123**, 7–15, https://doi.org/10.1016/j.dsr2.2015.07.014.

Kusahara, K., and K. I. Ohshima, 2009: Dynamics of the wind-driven sea level variation around Antarctica. *J. Phys. Oceanogr.*, **39**, 658–674, https://doi.org/10.1175/2008JPO3982.1.

Lewis, E. L., and R. G. Perkin, 1986: Ice pumps and their rates. *J. Geophys. Res.*, **91**, 11756, https://doi.org/10.1029/JC091iC10p11756.

Liu, Y., J. C. Moore, X. Cheng, R. M. Gladstone, J. N. Bassis, H. Liu, J. Wen, and F. Hui, 2015: Ocean-driven thinning enhances iceberg calving and retreat of Antarctic ice shelves. *Proc. Natl. Acad. Sci. USA*, **112**, 3263–3268, https://doi.org/10.1073/pnas.1415137112.

Losch, M., 2008: Modeling ice shelf cavities in a *z* coordinate ocean general circulation model. *J. Geophys. Res.*, **113**, C08043, https://doi.org/10.1029/2007JC004368.

MacAyeal, D. R., 1984: Thermohaline circulation below the Ross Ice Shelf: A consequence of tidally induced vertical mixing and basal melting. *J. Geophys. Res.*, **89**, 597–606, https://doi.org/10.1029/JC089iC01p00597.

Malyarenko, A., N. J. Robinson, M. J. Williams, and P. J. Langhorne, 2019: A Wedge mechanism for summer surface water inflow into the Ross Ice Shelf cavity. *J. Geophys. Res. Oceans*, **124**, 1196–1214, https://doi.org/10.1029/2018JC014594.

McKee, D. C., and D. G. Martinson, 2020: Wind-driven barotropic velocity dynamics on an Antarctic shelf. *J. Geophys. Res. Oceans*, **125**, e2019JC015771, https://doi.org/10.1029/2019JC015771.

Moholdt, G., L. Padman, and H. A. Fricker, 2014: Basal mass budget of Ross and Filchner-Ronne ice shelves, Antarctica, derived from Lagrangian analysis of ICESat altimetry. *J. Geophys. Res. Earth Surf.*, **119**, 2361–2380, https://doi.org/10.1002/2014JF003171.

Orsi, A. H., T. Whitworth, and W. D. Nowlin, 1995: On the meridional extent and fronts of the Antarctic circumpolar current. *Deep-Sea Res. I*, **42**, 641–673, https://doi.org/10.1016/0967-0637(95)00021-W.

Özsoy, E., 2020: *Geophysical Fluid Dynamics I: An Introduction to Atmosphere–Ocean Dynamics: Homogeneous Fluids.* Springer, 287 pp., https://doi.org/10.1007/978-3-030-16973-2.

Padman, L., M. R. Siegfried, and H. A. Fricker, 2018: Ocean tide influences on the Antarctic and Greenland ice sheets. *Rev. Geophys.*, **56**, 142–184, https://doi.org/10.1002/2016RG000546.

Prandtl, L., 1925: Bericht über untersuchungen zur ausgebildeten turbulenz. *Z. Angew. Math. Mech.*, **5**, 136–139, https://doi.org/10.1002/zamm.19250050212.

Pritchard, H., S. Ligtenberg, H. Fricker, D. Vaughan, M. van den Broeke, and L. Padman, 2012: Antarctic ice-sheet loss driven by basal melting of ice shelves. *Nature*, **484**, 502–505, https://doi.org/10.1038/nature10968.

Rignot, E., S. Jacobs, J. Mouginot, and B. Scheuchl, 2013: Ice-shelf melting around Antarctica. *Science*, **341**, 266–270, https://doi.org/10.1126/science.1235798.

Robertson, R., 2013: Tidally induced increases in melting of Amundsen Sea ice shelves. *J. Geophys. Res. Oceans*, **118**, 3138–3145, https://doi.org/10.1002/jgrc.20236.

Sansón, L. Z., and G. J. V. Heijst, 2002: Ekman effects in a rotating flow over bottom topography. *J. Fluid Mech.*, **471**, 239–255, https://doi.org/10.1017/S0022112002002239.

——, R. Serravall, G. F. Carnevale, and G. J. F. V. Heijst, 2005: Experiments and simulations on coastal flows in the presence of a topographic slope. *J. Phys. Oceanogr.*, **35**, 2204–2218, https://doi.org/10.1175/JPO2815.1.

Schaffer, J., R. Timmermann, J. Erik Arndt, S. Savstrup Kristensen, C. Mayer, M. Morlighem, and D. Steinhage, 2016: A global, high-resolution data set of ice sheet topography, cavity geometry, and ocean bathymetry. *Earth Syst. Sci. Data*, **8**, 543–557, https://doi.org/10.5194/essd-8-543-2016.

Steiger, N., E. Darelius, A. K. Wåhlin, and K. M. Assmann, 2021: Intermittent reduction in ocean heat transport into the Getz Ice Shelf cavity during strong wind events. *Geophys. Res. Lett.*, **48**, e2021GL093599, https://doi.org/10.1029/2021GL093599.

Stern, A. A., D. M. Holland, P. R. Holland, A. Jenkins, and J. Sommeria, 2014: The effect of geometry on ice shelf ocean cavity ventilation: A laboratory experiment. *Exp. Fluids*, **55**, 1719, https://doi.org/10.1007/s00348-014-1719-3.

Stewart, A. L., and A. F. Thompson, 2015: Eddy-mediated transport of warm circumpolar deep water across the Antarctic shelf break. *Geophys. Res. Lett.*, **42**, 432–440, https://doi.org/10.1002/2014GL062281.

Stewart, C. L., P. Christoffersen, K. W. Nicholls, M. J. Williams, and J. A. Dowdeswell, 2019: Basal melting of Ross Ice Shelf from solar heat absorption in an ice-front polynya. *Nat. Geosci.*, **12**, 435–440, https://doi.org/10.1038/s41561-019-0356-0.

St-Laurent, P., J. M. Klinck, and M. S. Dinniman, 2013: On the role of coastal troughs in the circulation of warm circumpolar deep water on Antarctic shelves. *J. Phys. Oceanogr.*, **43**, 51–64, https://doi.org/10.1175/JPO-D-11-0237.1.

Tenreiro, M., L. Z. Sansón, G. J. van Heijst, and R. R. Trieling, 2010: Experiments and simulations on self-organization of confined quasi-two-dimensional turbulent flows with discontinuous topography. *Phys. Fluids*, **22**, 025101, https://doi.org/10.1063/1.3313928.

Wåhlin, A. K., X. Yuan, G. Björk, and C. Nohr, 2010: Inflow of warm circumpolar deep water in the central Amundsen shelf. *J. Phys. Oceanogr.*, **40**, 1427–1434, https://doi.org/10.1175/2010JPO4431.1.

——, O. Kalén, K. M. Assmann, E. Darelius, H. K. Ha, T.-W. Kim, and S. H. Lee, 2016: Subinertial oscillations on the Amundsen Sea Shelf, Antarctica. *J. Phys. Oceanogr.*, **46**, 2573–2582, https://doi.org/10.1175/JPO-D-14-0257.1.

——, and Coauthors, 2020: Ice front blocking of ocean heat transport to an Antarctic ice shelf. *Nature*, **578**, 568–571, https://doi.org/10.1038/s41586-020-2014-5.

Walker, D. P., M. A. Brandon, A. Jenkins, J. T. Allen, J. A. Dowdeswell, and J. Evans, 2007: Oceanic heat transport onto the Amundsen Sea Shelf through a submarine glacial trough. *Geophys. Res. Lett.*, **34**, L02602, https://doi.org/10.1029/2006GL028154.

Williams, W. J., G. G. Gawarkiewicz, and R. C. Beardsley, 2001: The adjustment of a shelfbreak jet to cross-shelf topography. *Deep-Sea Res. II*, **48**, 373–393, https://doi.org/10.1016/S0967-0645(00)00085-0.